






## Early Holocene permafrost retreat in West Siberia amplified by reorganization of westerly wind systems

Ting-Yong Li <sup>1,2,11</sup>✉, Jonathan L. Baker <sup>3,11</sup>, Tao Wang<sup>2</sup>, Jian Zhang<sup>2</sup>, Yao Wu<sup>2</sup>, Hong-Chun Li <sup>4</sup>✉, Tatiana Blyakharchuk <sup>5</sup>✉, Tsai-Luen Yu<sup>4</sup>, Chuan-Chou Shen<sup>4</sup>, Hai Cheng <sup>3,6,7</sup>, Xing-Gong Kong <sup>8</sup>, Wen-Li Xie<sup>9</sup> & R. Lawrence Edwards<sup>8,10</sup>

Rapid permafrost degradation and peatland expansion occurred in Eurasia during the Early Holocene and may be analogous to the region's response to anthropogenic warming. Here we present a <sup>230</sup>Th-dated, multiproxy speleothem record with subdecadal sampling resolution from Kyok-Tash Cave, at the modern permafrost margin in the northern Altai Mountains, southwestern Siberia. Stalagmite K4, covering the period 11,400 to 8,900 years before present, indicates an absence of stable permafrost within three centuries of the Younger Dryas termination. Between 11,400 and 10,400 years ago, speleothem  $\delta^{18}\text{O}$  is antiphased between the Altai and Ural ranges, suggesting a reorganization of the westerly wind systems that led to warmer and wetter winters over West Siberia and Altai, relative to the zonally adjacent regions of Northern Eurasia. At the same time, there is evidence of peak permafrost degradation and peatland expansion in West Siberia, consistent with the interpreted climate anomaly. Based on these findings, we suggest that modern permafrost in Eurasia is sensitive to feedbacks in the ocean-cryosphere system, which are projected to alter circulation regimes over the continent.

<sup>1</sup>Yunnan Key Laboratory of Plateau Geographical Processes and Environmental Changes, Faculty of Geography, Yunnan Normal University, Kunming, China.

<sup>2</sup>Chongqing Key Laboratory of Karst Environment, School of Geographical Sciences, Southwest University, Chongqing, China. <sup>3</sup>Institute of Global Environmental Change, Xi'an Jiaotong University, Xi'an, China. <sup>4</sup>Department of Geosciences, National Taiwan University, Taipei, Taiwan. <sup>5</sup>Institute of monitoring of climatic and ecological systems of Siberian branch of Russian academy of sciences, Tomsk, Russia. <sup>6</sup>State Key Laboratory of Loess and Quaternary Geology, Institute of Earth Environment, Chinese Academy of Sciences, Xi'an, China. <sup>7</sup>Key Laboratory of Karst Dynamics, MLR, Institute of Karst Geology, CAGS, Guilin, China. <sup>8</sup>College of Geography Science, Nanjing Normal University, Nanjing, China. <sup>9</sup>State Key Laboratory for Mineral Deposits Research, Nanjing University, Nanjing, China. <sup>10</sup>Department of Earth Sciences, University of Minnesota, Minneapolis, MN, USA. <sup>11</sup>These authors contributed equally: Ting-Yong Li, Jonathan L. Baker. ✉email: [cdlity@163.com](mailto:cdlity@163.com); [hcli1960@ntu.edu.tw](mailto:hcli1960@ntu.edu.tw); [blyakharchuk@mail.ru](mailto:blyakharchuk@mail.ru)

Global warming since ~1880 C.E. has been the predominant feature of Earth's climate system and is attributed principally to anthropogenic increases in atmospheric carbon dioxide (CO<sub>2</sub>) and methane (CH<sub>4</sub>), as well as land-use changes<sup>1</sup>. The anthropogenic climate signal is prominent after ~1950 C.E., when the increase in surface temperature and sea level accelerated and began to exceed the range of Holocene variability<sup>2,3</sup>. Because of the disproportionate impact of warming on high-latitude regions, large freshwater and carbon storage in glaciers, permafrost, and peatlands are highly susceptible to abrupt warming<sup>4,5</sup>. Permafrost covers ~24% of the Northern Hemisphere land surface and stores an estimated 1700 Pg C, or double the atmospheric reservoir<sup>6</sup>. Surveys of Siberian permafrost in particular have recorded active-layer warming of 0.5–2 °C in recent decades<sup>7,8</sup>, shifting the discontinuous permafrost boundary northward and resulting in substantial landscape and hydrological changes<sup>9</sup>.

Thermal degradation of these natural sinks is likely to contribute positive feedbacks to climatic warming through albedo change, mobilization of soil carbon, and enhanced peatland methanogenesis<sup>10–14</sup>. The climatic response of Northern Eurasia to warming is complex, however, due to the interplay of several systems, such as midlatitude westerlies, the Siberian High, and to a lesser extent the Asian Summer Monsoon and East Asian Winter Monsoon<sup>15–19</sup>. Modern observations show spatiotemporal heterogeneities in permafrost warming and degradation that reflect both the longitudinal gradient in continentality and the influence of synoptic-scale circulation<sup>8</sup>. In Siberia, for example, permafrost warming slowed at multiple study areas during the 2000s, relative to 1970–1990 C.E., due to reductions or plateaus in local air temperature and snow-cover depth<sup>8</sup> that followed decadal-scale reversals in the strength of westerlies and the Siberian High<sup>20</sup>. Snow cover insulates ground temperatures from cold extremes<sup>21,22</sup>, so that long-term increases in winter precipitation also induce active-layer warming. Because

atmospheric circulation drives spatiotemporal climate trends<sup>23,24</sup>, which are superimposed on signals from radiative forcing, persistent changes in circulation modes can amplify or mitigate regional vulnerabilities to permafrost degradation<sup>25</sup>.

Feedbacks from recent perturbations to the ocean–cryosphere system, such as weakening of thermohaline circulation and sea-ice loss, have been linked to the divergence of winter climate with global warming trends in the continental midlatitudes, resulting in a “Warm Arctic–Cold Continent” pattern over Eurasia<sup>20</sup>. The dynamical links are still actively debated, with mixed support from models and observations<sup>26,27</sup>, but have significant implications for paleoclimate studies. For example, if past episodes of climatic warming, characterized by rapid sea-ice loss, resulted in similar modifications of atmospheric structure, a dampening of the winter climate response in northern Eurasia should be evident in high-resolution paleoclimate records. Attempts to better incorporate these dynamics into model forecasts and reconstructions have improved our understanding<sup>22,28–30</sup>, but high-resolution proxy data for validation of Holocene trends are still sparse in continental Eurasia<sup>15,31–34</sup>.

Abrupt warming in Eurasia following the Younger Dryas stadial may provide a plausible analog to 21st-century forecasts, because the Early Holocene (EH) was characterized by an abrupt increase in greenhouse-gas (GHG) content, sea level, and surface temperature, as well as Arctic sea-ice retreat<sup>35–39</sup>. High-latitude sea-surface temperature and summertime land-surface temperature likely exceeded the 20th-century mean<sup>2,3</sup>, due to maximal northern hemisphere summer insolation (NHSI) and enhanced oceanic poleward heat transport to the Arctic. Between 11.7 and 11.0 ka, Northern Eurasia experienced a spike in thermokarst activity<sup>40</sup>, accelerated degradation of alpine permafrost<sup>41</sup>, and a rapid expansion of West Siberian peatland<sup>11,42</sup>, resulting in enhanced riverine dissolved organic carbon (DOC) flux to the Arctic Ocean (4.5 Tg C y<sup>−1</sup> from the Lena watershed alone, or seven times modern levels<sup>43</sup>). Methane emissions from northern

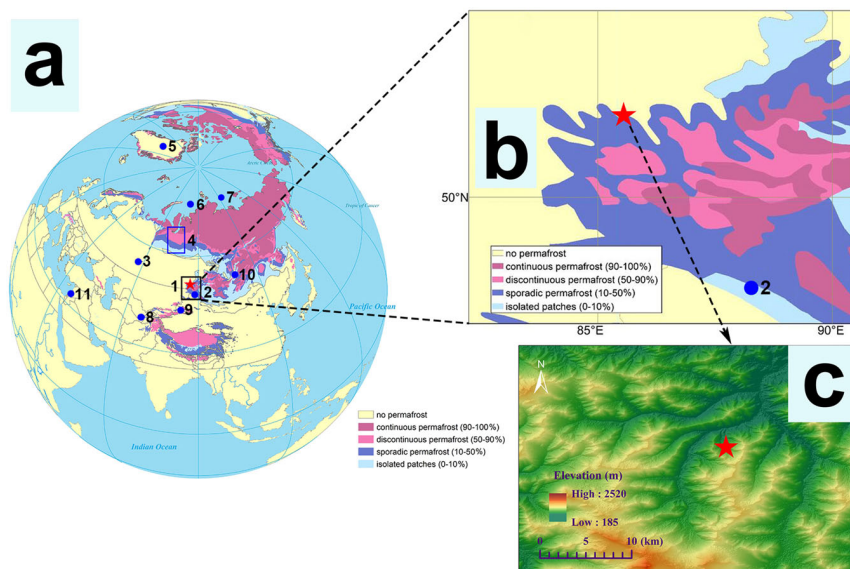


**Fig. 1 Study area and regional proxy records in relation to modern permafrost.** Location of Kyok-Tash Cave, southern Siberia, and other records compared in this study. **a** Type and distribution of permafrost in north hemisphere. Numbers indicate the locations of (1) Kyok-Tash Cave (51°43'33" N, 85°39'23" E) (this study); (2) Sahara Sand Peatland core (48°7' N, 88°21' E);<sup>15,33</sup> (3) Kinderlinskaya Cave (54°12' N, 56°54' E);<sup>32</sup> (4) West Siberian peatlands; (5) Greenland ice core (NGRIP) (75°6' N, 42°20' W); (6) Core BP00-36/04, Kara Sea (76°58' N 81°58' E); (7) Core P551/154, Laptev Sea (77°17' N 120°37' E). (8) Tonnel'naya Cave, Uzbekistan (38°24' N, 67°14' E);<sup>16</sup> (9) Kasang Cave, China (42°52' N, 81°45' E);<sup>16</sup> (10) Lake Baikal (~53°N 107°E); (11) Jeita Cave, Lebanon (33°57' N, 35°39' E). Records from sites 6–11 are plotted and discussed in the Supplementary Materials. **b** Amplification map near the location of Kyok-Tash Cave, located in the transition zone between discontinuous permafrost and non-permafrost regions. Numerals are the same as in **a**. **c** Digital elevation map of the local landscape. Kyok-Tash Cave is indicated by the red star.

peatlands were substantial from the YD to 8 ka and likely exceeded modern fluxes<sup>11</sup>. EH development of the West Siberia peatland, which is the largest today and stores 70 Pg C<sup>10</sup>, is attributed to an increase in warm-season moisture balance<sup>44</sup>, highlighting the role of atmospheric dynamics in determining the source-sink threshold. Understanding the mechanisms behind these EH trends is critical to constraining carbon-cycle feedbacks under future warming of the Eurasian permafrost regions.

Today, an estimated  $415 \pm 150$  Pg C is stored in northern peatlands<sup>5</sup>, which are projected to become a net source of CO<sub>2</sub> and CH<sub>4</sub> by 2100 C.E., due to permafrost thaw<sup>1,12</sup>. The southern margins are most vulnerable, and enhanced GHG release and thermokarst activity have already been observed in recent decades<sup>5</sup>. In addition to atmospheric C release through in situ methanogenesis and aerobic decomposition, Siberian peatlands are likely to contribute an excess of 2.7–4.3 Tg C y<sup>-1</sup> to the riverine DOC flux during the 21st century<sup>10</sup>. Major Siberian rivers currently deliver 17 Tg C y<sup>-1</sup> to the Arctic Ocean, partly from the leaching of soils in discontinuous permafrost but especially from permafrost-free peatland. The western bias in permafrost instability (Fig. 1A) is further evident in the disproportionately high contribution of riverine DOC from the Ob and Yenisey watersheds (West Siberia), in contrast to higher particulate organic matter from the eastern watersheds due to thermokarst activity<sup>13</sup>. Detailed paleoclimatic histories of the permafrost margins are therefore important to resolving the spatially complex response to modern warming<sup>34,45,46</sup>.

The disparity in regional dynamics between the EH and 21st century, however, precludes a direct comparison of the two scenarios. Due to changes in obliquity and precession, June and December insolation are now in opposite phase configurations, resulting in a steady reduction in the latitudinal insolation gradient—a driver of midlatitude circulation—since ~11 ka<sup>47</sup>. Continental ice sheets in Fennoscandia and North America were still large during the EH and strongly influenced continental climates<sup>32,48,49</sup>. Finally, EH warming occurred against a cooler background climate state, characterized by lower sea level, stronger land-sea thermal gradients, and a contrast in vegetative cover. It is critical, therefore, to delineate dynamic controls on EH climate change through high-quality paleoclimate data, before they can accurately inform 21st-century forecasts.

Herein we present a multiproxy speleothem record with sub-decadal resolution from Kyok-Tash Cave (KTC; 51°43′43″ N, 85°39′23″ E, 890 m a.s.l.), which is located in the northern slopes of the Altai Mountains, along the margin of the modern permafrost boundary (Fig. 1). Stalagmites can be absolutely and precisely dated by the <sup>230</sup>Th method and, combined with high-resolution geochemical data, can thereby provide detailed information about climate change in permafrost regions, including when liquid water became available<sup>45</sup>. Stalagmite K4, which grew between 11.4 and 8.9 ka B2K (kiloannum before 2000 C.E.; hereafter abbreviated as “ka”), was collected in situ from ~90 m depth (below entrance; Fig. S1) and measures 82 mm along the growth axis (Fig. S2a). The cave is not located within a protected nature reserve, and no federal or municipal permissions were required for collection. Permafrost is sporadic in the vicinity of the cave, where mean annual air temperature (MAAT) is 2.8 °C (1980–2010 C.E.), but its stability increases toward the south and east as a function of altitude and MAAT (Fig. 2B). This region is highly sensitive to anthropogenic warming over the past century, which has led to substantial reductions in glacier mass<sup>50</sup> that will likely continue under 21st-century emissions scenarios<sup>4</sup>. The MAAT across 15 meteorological stations increased by 1.85 °C (0.41 °C per decade) from 1970–2015 C.E.<sup>51</sup>, which is nearly twice the global mean. Warming was strongest in spring (0.64 °C per decade) and weakest in winter (0.27 °C per decade), and the trend

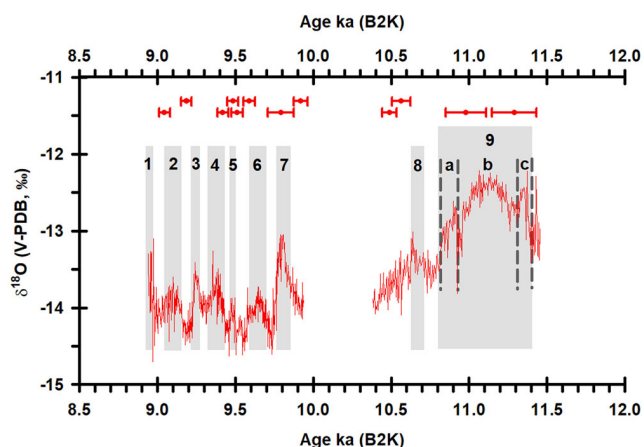


**Fig. 2 High-frequency  $\delta^{18}\text{O}$  variations in stalagmite K4.** Vertical shaded bars and numerals denote positive  $\delta^{18}\text{O}$  excursions identified in the KTC record. The broad excursion 9 is divided further into three substages. Each <sup>230</sup>Th date utilized in the age model is labeled by a red dot (mean age) with 2- $\sigma$  error bars.

is associated with regional geopotential height (GPH) anomalies that enhanced southwesterly circulation<sup>23,51</sup>. Based on our analysis of local weather data, Global Network of Isotopes in Precipitation (GNIP) stations, and modeled  $\delta^{18}\text{O}$  of precipitation ( $\delta^{18}\text{O}_p$ ), we find that regional climate and moisture trajectories are strongly correlated to teleconnection indices describing westerly wind systems over northern Eurasia. The location of KTC and nature of the proxy are thus ideal to constrain the dominant climate dynamics associated with permafrost degradation in the Altai Mountains and peatland development in West Siberia during the EH.

## Results

**Age model.** The age and growth rate of stalagmite K4 are constrained by 12 <sup>230</sup>Th ages, which are summarized in Supplementary Table 1 along with isotopic compositions of U and Th. Concentrations of <sup>238</sup>U and <sup>232</sup>Th range from 1.2 to 3.2 ppm and from 0.03 to 20 ppb, respectively, and <sup>230</sup>Th/<sup>232</sup>Th ratios range from 228 to 86,506 ( $\times 10^{-6}$ ), yielding high-precision ages. Individual 2- $\sigma$  uncertainties ranged from 0.36 to 1.26% (average 0.6%), which translates to  $\pm 33$  y at 9.2 ka and  $\pm 142$  y at 11.3 ka. All <sup>230</sup>Th ages are in stratigraphic order. The age-growth model for K4 was constructed using MOD-AGE software<sup>52</sup> (Fig. S2b), which interpolates between <sup>230</sup>Th dates and estimates age uncertainty using a Monte Carlo simulation. Based on the MOD-AGE results for K4, speleothem growth initiated at  $11.45 \pm 0.2$  ka, within 2- $\sigma$  model uncertainty of the Younger Dryas termination. Growth continued until  $8.92 \pm 0.06$  ka, with the exception of a ~440-year hiatus from 10.38 to 9.94 ka (55.0–55.1 mm depth), which is clearly visible in the stratigraphy and associated with a growth-axis shift (Fig. S2a). The bounding layers do not exhibit stable-isotope or trace-element anomalies; hence, it is unclear from geochemical data and visual inspection whether the change in drip position resulted from a climatic influence.

**Stable-isotope composition and fluctuations.** A total of 819 paired  $\delta^{13}\text{C}$  and  $\delta^{18}\text{O}$  analyses were performed on micromilled powders from K4 along the 82 mm growth axis, yielding a mean temporal resolution of 2.5 years according to the age model (Fig. 2 and Supplementary Data 1). To the best of our knowledge, this sampling resolution is unprecedented for paleoclimatic records from Eurasia spanning the EH. Values of  $\delta^{18}\text{O}$  range from -12.0 to -14.7‰ Vienna Pee Dee Belemnite (V-PDB),



with an average of  $-13.7\text{‰}$ . The uppermost 0.8 mm of K4 has been excluded from plots, because it exhibits a 2.6 and 4.2‰ positive shift in  $\delta^{18}\text{O}$  and  $\delta^{13}\text{C}$ , respectively, characteristic of kinetic fractionation during cessation of the drip and stalagmite growth (Supplementary Data 1). Centennial-scale shifts up to 1.5‰ are common throughout the record, particularly in the latter half. Variance in  $\delta^{18}\text{O}$  is higher from 11.45 to 10.38 ka than from 9.94 to 8.93 ka at a ratio of  $\sim 1.3$ , but with a lower AR(1) coefficient of 0.66 (vs. 0.88).

Mean  $\delta^{18}\text{O}$  in K4 is higher during the Preboreal Stage ( $-13.1\text{‰}$ ) than the Boreal Stage ( $-14.0\text{‰}$ ), separated by the hiatus from 10.38 to 9.94 ka. Amid the overall negative trend from bottom to top, we identified nine significant positive  $\delta^{18}\text{O}$  excursions, enumerated 1–9 in Fig. 2 from youngest to oldest. The magnitude of each excursion exceeds 1‰. Event 9 was the longest event, lasting from 11.4 to 10.7 ka, and is subdivided into three shorter  $\delta^{18}\text{O}$  events (a, b, and c) that occurred from 10.93 to 10.81 ka, 11.31 to 10.93 ka, and 11.39 to 11.31 ka, respectively (Fig. 2). The midpoints of  $\delta^{18}\text{O}$  events 2–8 are 9.11, 9.24, 9.36, 9.48, 9.65, and 9.80 ka, respectively, with each event lasting 50–150 years (Fig. 2). Event 1 began at 8.99 ka and lasted  $\sim 50$  years, after which stalagmite growth ceased.

Values of  $\delta^{13}\text{C}$  range from  $-10.56$  to  $-7.01\text{‰}$  V-PDB (mean =  $-9.43\text{‰}$ ), with the exception of anomalously  $^{13}\text{C}$ -rich subsamples in the uppermost 2 mm (Supplementary Data 1). Variance in  $\delta^{13}\text{C}$  is much lower from 11.45 to 10.38 ka than from 9.94 to 8.93 ka (ratio = 0.12), but with a higher AR(1) coefficient of 0.81 (vs. 0.69). This contrast in signal behavior across the EH is opposite that of  $\delta^{18}\text{O}$ . Speleothem  $\delta^{13}\text{C}$  is apparently more stable with slightly lower values during the Preboreal Stage (mean =  $-9.7\text{‰}$ ) than the Boreal Stage (mean =  $-9.3\text{‰}$ ); however, no long-term trend can be distinguished. Although  $\delta^{13}\text{C}$  and  $\delta^{18}\text{O}$  exhibit a weak anticorrelation across the entire length of K4 ( $r = -0.18$ ), the relationship is positive and highly significant from 11.45 to 10.38 ka ( $r = 0.71$ ;  $p < 0.001$ ). Because the magnitude of  $\delta^{13}\text{C}$  changes across this interval is minimal compared to  $\delta^{18}\text{O}$ , kinetic fractionation is not a likely driver of the coupled behavior<sup>53,54</sup>.

**Modern climatology of the northern Altai region and controls on  $\delta^{18}\text{O}_p$ .** The closest weather station to KTC is Kyzyl-Ozyk ( $51.9^\circ\text{N}$   $86.00^\circ\text{E}$ , 400 m a.s.l.), located  $\sim 30$  km to the northeast (station data accessed from [meteo.ru/data](http://meteo.ru/data)). Climate is highly continental (Fig. S3), with seasonal air temperature varying from  $-12.5$  (DJF) to  $17.3^\circ\text{C}$  (JJA) and precipitation from 27 mm (DJF) to 101 mm per month (JJA). The MAAT ranges from  $-1.01$  to  $4.53^\circ\text{C}$  in the dataset, which spans 1940–2018 C.E., whereas mean annual precipitation ( $P_{\text{ann}}$ ) is 731 mm (1980–2010 C.E.) and varies from 521 to 912 mm since 1966 C.E. Potential evapotranspiration (PET), estimated by the Thornthwaite method<sup>55</sup>, is up to 27 mm higher than monthly precipitation from May to August (Fig. S3). The summer deficit is partially offset by antecedent moisture from spring snowmelt, however, and the annual moisture balance is positive ( $P_{\text{ann}} - \text{PET}_{\text{ann}} = 175$  mm).

To evaluate the influence of major teleconnections on local climate, we analyzed monthly  $T$  and  $P$  from a total of 12 weather stations within 400 km (Fig. S4). Each dataset extends to 2018 C.E. from at least 1950 C.E., which is the common length of the indices, calculated from the National Centers for Environmental Prediction/National Center for Atmospheric Research reanalysis<sup>56</sup>. All 12 stations exhibit similar seasonal  $T$  patterns, with the exception of lower  $T$  at high-altitude sites Ust'-Koksa and Kara-Tyurek to the southeast. Monthly  $P$  is ubiquitously higher in summer than winter for 11 stations, whereas Nenastnaya station exhibits higher autumn to early-

winter precipitation, comparable to the Trans-Ural region. Stations with higher annual  $P$  tend to be located on windward northern and western macroslopes of the Altai Mountains, due to orographic rainout of the more humid westerly air masses.

For each dataset, Pearson correlation coefficients ( $r$ ) were calculated between each month (plus the DJF mean) and the Scandinavian pattern (SCAN), the Arctic oscillation (AO), the North Atlantic oscillation (NAO), the East Atlantic/West Russia Pattern (EAWR), and the Siberian High Index (SHI; identified only as a DJF mean) (Fig. S5). Surface-air temperature (SAT) is strongly anticorrelated with SCAN for all months, meaning that lower SAT near the cave site is associated with Rossby-wave propagation downstream from a lower-tropospheric ridge centered over Scandinavia<sup>57</sup>. The correlation between warm-season precipitation and SCAN is weak, but consistently positive across all stations, which is likely a function of negative GPH anomalies associated with SCAN+ in the absence of the Siberian High. No significant correlation to the NAO was detected, except with the DJF mean  $T$  for some stations, which highlights the importance of not generalizing midlatitude westerly strength from the NAO index alone<sup>58</sup>. Conversely, both the AO and EAWR exhibit moderate influence on SAT, which is strongest during the winter half year. In their negative state, these teleconnections are expressed by enhanced Rossby-wave amplitude and wave-train features, which are conducive to the intrusion of high-latitude air masses to central Eurasia<sup>59</sup>. All stations exhibit a negative correlation between DJF precipitation and the SHI, indicating that a weakened Siberian High allows for southwesterly flow into the Altai region, consistent with analysis of circulation regimes<sup>23</sup>.

Nearby GNIP stations at Barabinsk ( $53.3^\circ\text{N}$   $78.4^\circ\text{E}$ ) and Novosibirsk ( $55.0^\circ\text{N}$   $82.9^\circ\text{E}$ ) provide a first-order estimate of  $\delta^{18}\text{O}_p$  at KTC. The datasets are extremely limited, as monthly  $\delta^{18}\text{O}_p$  is only available for 1990 C.E. at Novosibirsk and for 1–4 years from 1996 to 2000 C.E. at Barabinsk. Monthly weighted mean annual  $\delta^{18}\text{O}_p$  at Novosibirsk and Barabinsk stations is  $-14.1$  and  $-11.3\text{‰}$ , respectively, and reflects the high inter-annual and seasonal variability of the region due to moisture source<sup>58</sup>. These values adjust to  $-17.8$  and  $-16.7\text{‰}$  after accounting for PET (Fig. S3), which more plausibly represents the seasonally biased infiltration that is typical of temperate sites<sup>32,60</sup>. To evaluate climatic controls at multidecadal scale, modeled  $\delta^{18}\text{O}_p$  from 1979 to 2016 C.E. was retrieved from the IsoGSM2 database<sup>61</sup> for the two grid points adjacent to KTC. Monthly mean values are nearly identical to data from Barabinsk Station for the warm season ( $\Delta\delta^{18}\text{O}_p = -0.2\text{‰}$ ; May to Oct) but are 2.5‰ higher for colder months (Nov to Apr). Monthly weighted  $\delta^{18}\text{O}_p$  in the IsoGSM2 dataset was  $-10.5\text{‰}$ , or  $-14.3\text{‰}$  after subtracting PET (Fig. S3).

Finally, we compared modeled  $\delta^{18}\text{O}_p$  from 1979 to 2016 C.E. with major teleconnections and climate variables (Fig. S6). Monthly  $\delta^{18}\text{O}_p$  near KTC is significantly correlated with SAT and GPH, except for June, July, and September (Fig. S3f). The dependence of both SAT and  $\delta^{18}\text{O}_p$  on synoptic winter (DJF) circulation mode is evident in gridded correlation maps (Fig. S7), which illustrate the relationship with GPH (500 mb) anomalies and explain the correlations to the AO, SHI, and SCAN—all associated with wave-train features over northern Eurasia. The Scandinavian pattern shows the strongest influence on local  $\delta^{18}\text{O}$  and SAT, as it modifies the wave structure downstream across northern Eurasia<sup>57</sup>, followed by the Siberian High, a surface-level blocking feature that overlaps our study region. Notably, the loading pattern of the AO (a hemispheric anomaly) intersects with our correlation map only in the North Atlantic sector, resulting in weakly significant covariance during the coldest months.

**Paleoclimatic significance of stalagmite  $\delta^{18}\text{O}$  at KTC.** Oxygen-isotope data from KTC are a plausible proxy for changes in regional temperature, atmospheric structure, and moisture source during the EH<sup>32,62</sup>. Precipitation of calcite proceeds from the degassing of  $\text{CO}_2$  from drip water, which originates from local meteoric water that infiltrates through the vadose zone above the cave. Speleothem  $\delta^{18}\text{O}$  thus inherits the climate signal imprinted on local precipitation due to changes in moisture source, SAT along air trajectories (modulating fractionation during Rayleigh distillation), and net infiltration as a function of P/PET balance<sup>62,63</sup>. This signal is modified by a T-dependent fractionation and kinetic effects<sup>54</sup>, but cave-air temperature follows local MAAT<sup>62,64,65</sup>, and we found no evidence of strong kinetic controls apart from the uppermost 2 mm of K4. Thermal modeling<sup>66</sup> and modern observations<sup>64,67</sup> show that cave-air and dripwater temperature can lag changes in surface climate by about a century at the depth from which K4 was collected (~90 m; Fig. S1) and that the response is dampened (nonlinear). We emphasize, however, that this phenomenon affects only the relative amplitude of  $\delta^{18}\text{O}$  excursions, but not the shape of the signal or its link to  $\delta^{18}\text{O}_\text{p}$ . Similarly, apart from substantial changes in kinetic fractionation over time, only the absolute values of speleothem  $\delta^{18}\text{O}$  are affected (becoming less negative), thus preserving the relative changes in  $\delta^{18}\text{O}_\text{p}$  associated with atmospheric dynamics. However, several lines of evidence point to the precipitation of K4 near equilibrium. First, KTC has only a vertical-shaft entrance, and K4 was collected from a deep passage that is isolated from seasonal ventilation effects on T and RH (Fig. S1). Second,  $\delta^{18}\text{O}$  data do not covary with  $\delta^{13}\text{C}$  or Mg/Ca, which might be expected under strong disequilibrium, and overall variance in  $\delta^{13}\text{C}$  is lower than that of  $\delta^{18}\text{O}$ . Third, the low speleothem  $\delta^{18}\text{O}$  values observed in K4 (below) are incompatible with a strong positive shift from kinetic effects. Finally, a “replication test” for K4 is satisfied by comparison with regional trends (see “Discussion”).

Despite higher monthly precipitation at KTC during the warm season, the P–PET balance is negative during peak summer months, suggesting that dripwater  $\delta^{18}\text{O}$  disproportionately reflects the infiltration of cold-season precipitation (Fig. S3). This theoretical bias, observed in the Ural Mountains<sup>32</sup>, is consistent with K4  $\delta^{18}\text{O}$  data. If we assume calcite precipitation near equilibrium<sup>54</sup> and dripwater temperatures between 0°C and modern MAAT (1.5–3°C), then dripwater  $\delta^{18}\text{O}$  ranged from –18.6 to –15.6‰ during the EH, which envelops amount-weighted estimates for modern  $\delta^{18}\text{O}_\text{p}$  after accounting for PET (“Modern climatology of the northern Altai region and controls on  $\delta^{18}\text{O}_\text{p}$ ”). Assuming disequilibrium, then the estimated EH  $\delta^{18}\text{O}_\text{p}$  of drip water would be even lower by the magnitude of kinetic fractionation. We may conclude, therefore, that K4  $\delta^{18}\text{O}$  is a stronger proxy for winter half-year  $\delta^{18}\text{O}_\text{p}$  than amount-weighted annual  $\delta^{18}\text{O}_\text{p}$ , with the caveat that cooler/wetter summers and/or winter aridity in the past could have increased the contribution of warm-season precipitation to the aquifer, shifting values positive.

Although local GNIP data are too sparse to resolve interannual controls on  $\delta^{18}\text{O}_\text{p}$ , our analysis of monthly IsoGSM2 data suggests that the AO and SCAN simultaneously influence SAT and  $\delta^{18}\text{O}_\text{p}$  at KTC, particularly the DJF mean, with similar results for Kinderlinskaya Cave<sup>32</sup> (KC; Fig. S6). This positive  $\delta^{18}\text{O}_\text{p}$ –SAT relationship (the “temperature effect”)<sup>68</sup> is corroborated by observations from the Baikal and Altai region<sup>15,69</sup>, isotope-enabled modeling of recent precipitation in West Siberia<sup>70</sup>, a global analysis of the last millennium<sup>71</sup>, LGM–Holocene experiments<sup>31</sup>, and by regional paleoclimate studies<sup>32,33</sup>. Moisture transport to KTC by stronger (weaker) westerlies can also decrease (increase) the moisture-source latitude due to the mean position of the jet stream, causing local  $\delta^{18}\text{O}_\text{p}$  to become less

(more) negative<sup>69,72</sup> (Fig. S8a, b). When the AO (SCAN) is in the negative (positive) phase—reflecting a weakened westerly state—enhanced Rossby-wave amplitude further increases the effective continentality of the site while reducing the mean SAT along air trajectories, both of which contribute to a higher integrated Rayleigh distillation and lower  $\delta^{18}\text{O}_\text{p}$  (Fig. S8b). If groundwater contributions from summer rainfall were substantially higher during the EH, it could potentially dampen the T signal by weakening the correlation between winter T and annual  $\delta^{18}\text{O}_\text{p}$ <sup>58,70</sup>. Lack of a clear temperature effect during summer is explained by the influence of recycled continental moisture, which can account for half of summer Siberian rainfall<sup>72</sup>. It is therefore crucial to test for strong deviations in hydroclimate, relative to the observational period and model scenarios, through additional proxies.

Absolute temperature changes cannot be quantified directly from K4  $\delta^{18}\text{O}$ , due to uncertainties in the EH  $\delta^{18}\text{O}_\text{p}$ –T relationship and seasonal moisture balance, but modern observations and regional paleoclimate records provide reasonable constraints. If we assume a long-term  $\delta^{18}\text{O}$ –T slope between 0.63‰°C<sup>–1</sup> (composite for European GNIP stations<sup>73</sup>) and 0.50‰°C<sup>–1</sup> (modeled winter relationship for West Siberia<sup>70</sup>), offset by –0.21‰°C<sup>–1</sup> from calcite precipitation<sup>54</sup>, the 2‰ range in smoothed K4  $\delta^{18}\text{O}$  (Fig. 3) reflects EH temperature variability up to 4.8–6.9°C. A recent calibration based on precipitation events and trajectory modeling for Irkutsk, Siberia supports the low end of the range (0.50‰°C<sup>–1</sup>) and is recommended for paleoclimate studies in this region<sup>69</sup>. Their observations are in line with the orbital-scale slope for DJF air temperatures over Siberia (0.53‰°C<sup>–1</sup>), using the ECHAM5-wiso model to simulate scenarios from LGM to RCP4.5<sup>31</sup>. We consider this  $\Delta T$  estimate, which is ~2–3 times the magnitude of recent anthropogenic warming and comparable to total Holocene warming in Altai<sup>74</sup>, to be an unlikely—yet plausible<sup>75</sup>—theoretical maximum. For example, any increase (decrease) in the relative contributions from JJA (DJF) precipitation would decrease the estimated temperature variance. Persistent shifts in mean circulation regime or moisture source can further amplify  $\delta^{18}\text{O}$  variance in excess of the assumed  $\delta^{18}\text{O}$ –T slope<sup>76</sup>. In addition, the SAT change inferred from  $\delta^{18}\text{O}$  variability is biased toward the predominantly winter source of drip water, and the MAAT signal could have been muted by trends in other seasons, such as documented summer warming from 11 to 9 ka<sup>17</sup>.

Given these relationships and constraints, we contend that speleothem  $\delta^{18}\text{O}$  data in KTC may elucidate the role of atmospheric circulation in driving EH changes over southwestern Siberia and the Altai region. Cold-season GPH structure, captured by the SCAN and AO indices, is strongly imprinted on the local  $\delta^{18}\text{O}$  of infiltrating water, which is biased toward winter precipitation. Positive (negative)  $\delta^{18}\text{O}$  anomalies in the K4 isotope record are interpreted to reflect warmer (colder) winter air temperatures, associated with predominantly southwesterly (northwesterly) circulation to the region.

**Atmospheric circulation changes during the EH.** As a proxy for the isotopic composition of moisture transported to the Altai region, temporal variability in K4  $\delta^{18}\text{O}$  reflects predominant circulation regimes over northern Eurasia and concomitant shifts in regional winter SAT. Direct comparison to the southern Ural speleothem record (KC; Fig. 3), however, reveals a complex EH evolution of winter air circulation over southern Siberia. From 9.94 to 8.93 ka, centennial  $\delta^{18}\text{O}$  variability in KC and KTC is in phase and systematically offset by ~1.2‰, due to the increased continentality and elevation of KTC. This covariation suggests that regional winter climate shifts across the interval were

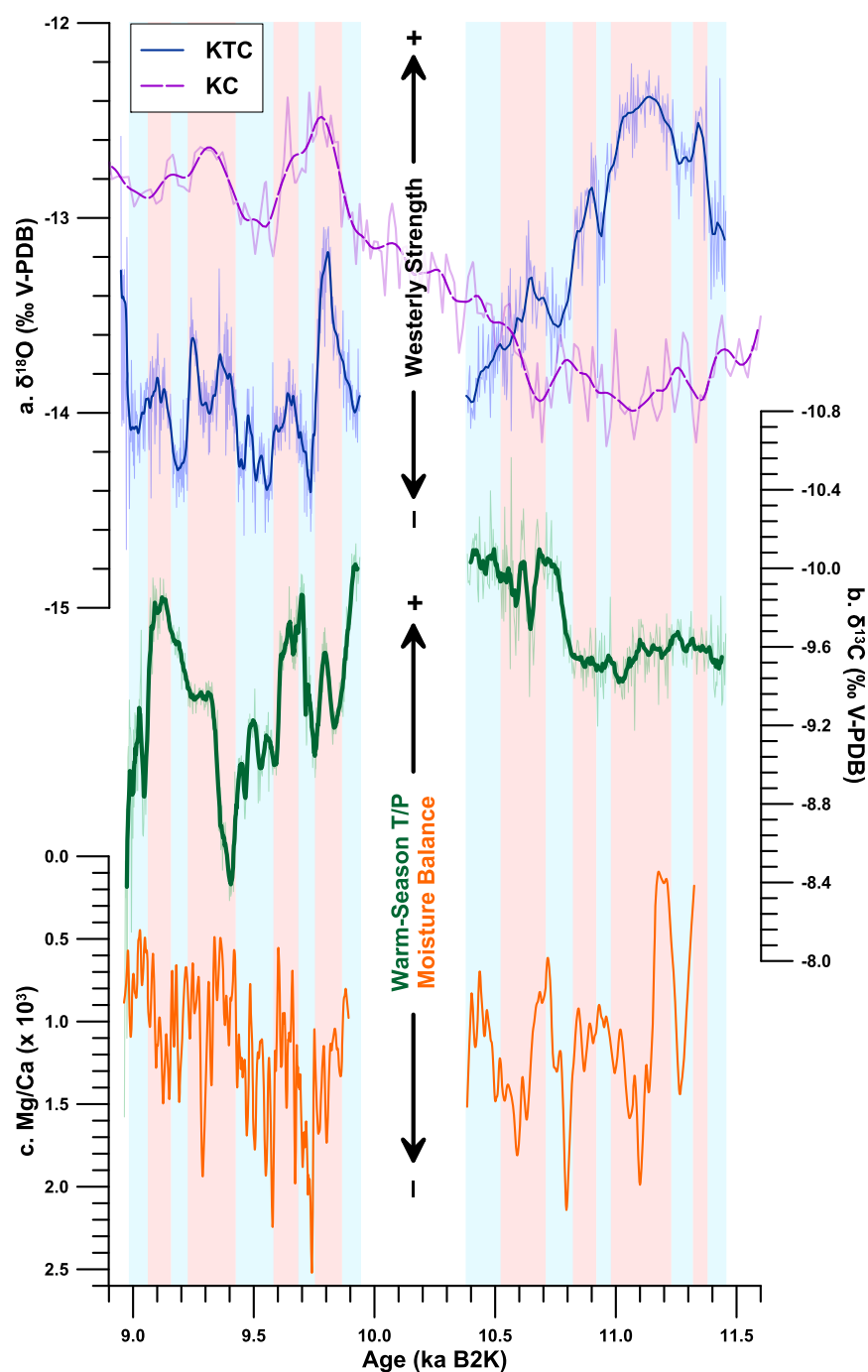


**Fig. 3** Multiproxy interpretation of Early Holocene circulation and regional climate. **a** Speleothem  $\delta^{18}\text{O}$  data from KTC (solid blue) and KC (dashed purple). **b** KTC  $\delta^{13}\text{C}$ . **c** KTC Mg/Ca. Bold lines represent a 15-point LOESS smoothing of each dataset. Red and blue shading are defined by positive and negative  $\delta^{18}\text{O}$  anomalies, respectively, in K4.

analogous to the modern SCAN/AO influence on SAT and  $\delta^{18}\text{O}_p$  at each cave site (Fig. S6). Excursions 1–7 identified in K4  $\delta^{18}\text{O}$  (Fig. 2) are generally evident in KC  $\delta^{18}\text{O}$ , albeit at lower resolution (Fig. 3). These multidecadal–centennial-scale events thus correspond to strengthened westerly circulation and positive winter  $T$  anomalies over a large sector of northern Eurasia.

In the earlier half of the K4 record (Events 8–9; 11.45–10.38 ka),  $\delta^{18}\text{O}$  is highly anticorrelated between KC and KTC (Fig. 3), even for short-term excursions. We infer from the strong relationship that the winter climate signal is well preserved in K4  $\delta^{18}\text{O}$ , but the sign reversal indicates a fundamental shift in

atmospheric structure and predominant circulation regime. The broad positive excursion centered at ~11.1 ka suggests enhanced southwesterly flow to Altai region, contrasted with north-meridional flow to the southern Ural Mountains (Fig. S8c). This disparity cannot be explained by analogy to the modern SCAN/AO pattern. Rather, we attribute it to millennial-scale weakening of the Siberian High and Ural blocking, which are linked in the modern climatology<sup>77</sup>. The SHI strongly influences winter  $\delta^{18}\text{O}_p$  and SAT at KTC, but not at KC (Fig. S6). Atmospheric blocking in the Ural region further leads to antiphasing of both  $\delta^{18}\text{O}_p$  and SAT between the cave sites (Fig. S9). Therefore, positive

(negative)  $\delta^{18}\text{O}$  anomalies at KTC (KC) are consistent with a shift in blocking frequency from the Ural sector to Scandinavia and the northeastern North Atlantic. Peak values near 11.1 ka are coincident with the Preboreal oscillation (Meltwater Pulse 1B), a period of enhanced meltwater contribution to high-latitude oceans and perturbations to North Atlantic currents<sup>78</sup>, as well as rapidly retreating Arctic sea ice and advancing/warming coastlines<sup>37,43,79,80</sup>. The Scandinavian Ice Sheet (SIS) remained sufficiently large to modify atmospheric flow after the YD-EH transition and, coincidentally, its final collapse by 9.7 ka<sup>49</sup> corresponds to the sign reversal in the KTC–KC  $\delta^{18}\text{O}$  relationship (Fig. 3). In light of recent modeling<sup>29</sup>, it is plausible that the contrast of a still glaciated landscape with Arctic warming until ~10 ka modified the overlying GPH structure in a way that significantly shifted atmospheric blocking patterns. The result was an early and abrupt amelioration of climate in West Siberia and the Altai region, relative to continental western Eurasia<sup>32</sup>. We consider the regional context further in the Supplementary Materials (Fig. S10).

## Discussion

Climatic warming of Eurasian permafrost regions during the EH was characterized by a millennial-scale shift in dominant atmospheric mode, which created favorable conditions for rapid permafrost degradation in the northern Altai region and the abrupt expansion of West Siberian peatlands. Initiation of speleothem growth at KTC confirms the infiltration of liquid karst waters through discontinuous permafrost by ~11.5 ka, suggesting that MAAT crossed the  $-2^\circ\text{C}$  threshold within two centuries of the abrupt GHG increase following the YD termination<sup>10,45</sup> (Fig. 4). Despite the more continental setting and higher elevation than KC (890 vs. 240 m a.s.l.), the onset of stalagmite growth at KTC is within age-model uncertainty of the Ural cave site<sup>32</sup>, with a probable lag of only ~200 years. However, it precedes the earliest documented Holocene growth in Okhotnichya (52.1°N 105.5°E, 700 m a.s.l.) and Botovskaya (55.3°N 105.3°E, 750 m a.s.l.) caves by ~1450 years<sup>45,46</sup>. This zonal heterogeneity is not plausibly explained by radiative forcing alone (e.g., from insolation or GHGs), but reflects the sensitivity of each region to climatic feedbacks affecting heat/moisture transport to the continental interior<sup>29,30,34</sup>.

Based on the inverse relationship between KTC and KC  $\delta^{18}\text{O}$  during the earliest Holocene, we have attributed the positive peak in K4  $\delta^{18}\text{O}$  to weakening of the Siberian High and a concomitant reduction in Ural blocking frequency from ~11.4 to 10.5 ka, which is corroborated by low  $\text{K}^+$  concentration in GISP2<sup>81</sup>. Permafrost degradation accelerated within the same interval at Central and East Asian sites marginal to Siberian High influence, supporting our interpretation<sup>41,79,80</sup>. This reorganization of westerly wind systems would have enhanced southwesterly flow to West Siberia and the Altai region—relative to western Russia and Central Siberia—which could explain why winter SAT and  $P$  in the Lake Baikal region remained depressed around 11 ka<sup>82</sup>. Abrupt warming in and a marked increase in precipitation occurred at Lake Baikal and in the high-altitude eastern Altai around 10 ka<sup>82,83</sup>, consistent with the observed E–W lag in the resumption of speleothem growth. Modern permafrost distribution captures a similar zonal heterogeneity (Fig. 1A). Permafrost regions of the Altai Mountains and West Siberia are thus more imminently susceptible to abrupt warming associated with GHG increases and Arctic amplification.

Early permafrost degradation in the northern Altai Mountains is further evidenced by afforestation of the Ulagan Plateau—located 170 km southeast of KTC—from 12 to 9.5 ka<sup>84</sup>. A review of pollen records from the Altai-Sayan range and the southern

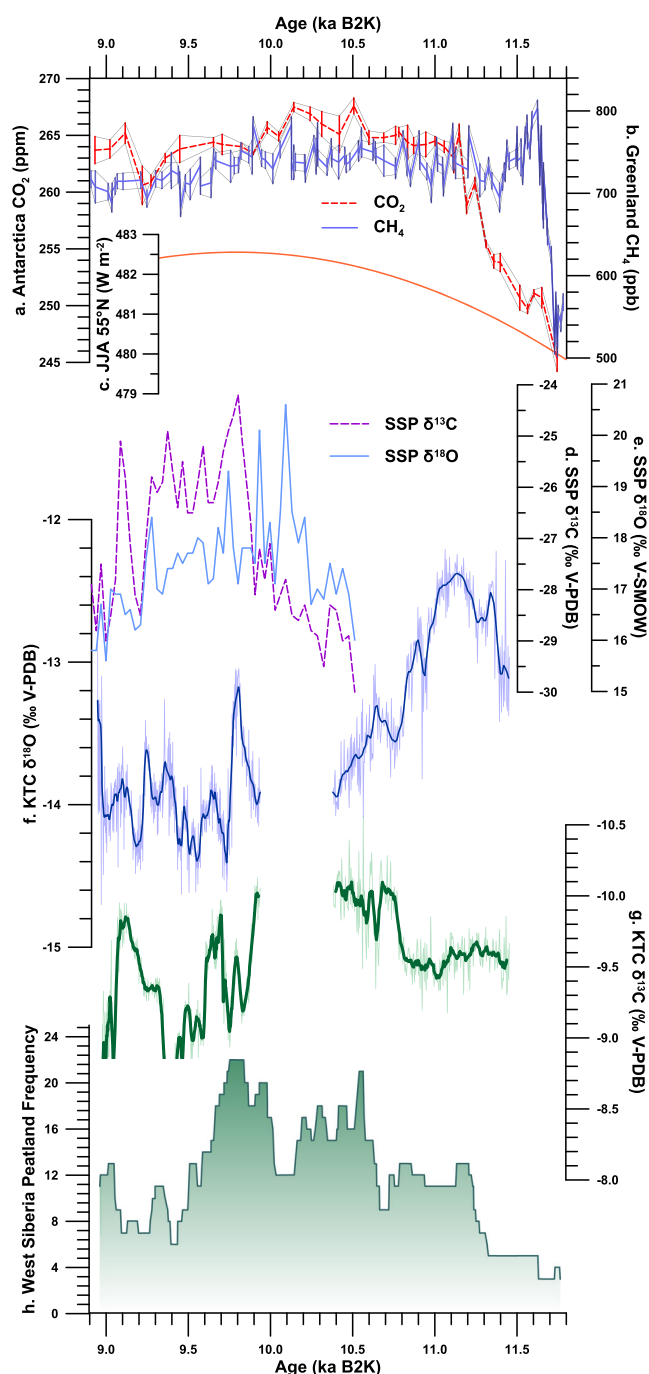


**Fig. 4 Climatic and permafrost response in West Siberia to Early Holocene forcings.** Comparison of stalagmite K4 with regional proxy records and forcings. High-resolution composites of **a** atmospheric  $\text{CO}_2$  in Antarctic ice cores<sup>38</sup> (dashed red); and **b** atmospheric  $\text{CH}_4$  in Greenland ice cores<sup>39</sup> (solid blue). Error bars denote the reported  $2\sigma$  analytical uncertainty. **c** Summer (JJA) insolation at  $55^\circ\text{N}$ . Sahara Sand Peatland record of cellulose **d**  $\delta^{13}\text{C}$ , a proxy for summer  $T^{17}$  (dashed purple); and **e**  $\delta^{18}\text{O}$ , a proxy for winter  $T^{33}$  (solid light blue). **f** K4  $\delta^{18}\text{O}$  (light blue; this study) with 15-point LOESS smoothing (bold line). **g** K4  $\delta^{13}\text{C}$  (light green; this study) with 15-point LOESS smoothing (bold line). **h** Frequency of basal peat core ages in West Siberia<sup>42</sup>. The geographical locations of proxy records are shown in Fig. 1, excepting the Antarctic ice cores.



Siberia lowlands documented widespread ecological transitions by 11 ka, associated with positive temperature anomalies that were absent to the south and east (Tianshan and Hangay ranges<sup>85</sup>). Pollen data are corroborated by stable-isotope evidence for EH warming in Altai<sup>15,17,33</sup>. Replacement of tundra by steppe and taiga assemblages characterized EH changes in the southern Altai, including a  $\sim 4^\circ\text{C}$  winter  $T$  spike near 11 ka<sup>75</sup>. These ecological shifts are consistent with K4  $\delta^{13}\text{C}$  values, which range from  $-9.5$  to  $-10.1\text{‰}$  in the early half of the record (Fig. 3). For cave sites where MAAT is  $<5^\circ\text{C}$ , a mean  $\delta^{13}\text{C}$  of  $-9.7\text{‰}$  is exceptionally low (second only to KC)<sup>53</sup>. Low  $\delta^{13}\text{C}$  values from the very beginning of the record suggest relatively dense vegetation, sufficient SAT and moisture balance, as well as uniquely open-system conditions that allow exchange with soil-respired  $\text{CO}_2$  during karst dissolution.

Speleothem  $\delta^{13}\text{C}$  is further decoupled from Mg/Ca over the recorded interval (Fig. 3b, c). This lack of covariance suggests that common non-climatic controls on  $\delta^{13}\text{C}$ —kinetic fractionation, evaporation, or prior calcite precipitation in the drip/epikarst<sup>53,62</sup>—cannot explain the low-frequency signal in either proxy. We thus refer to the paired series to rule out strong deviations in hydroclimate or kinetic controls that might undermine our interpretation of  $\delta^{18}\text{O}$  (see “Paleoclimatic significance of stalagmite  $\delta^{18}\text{O}$  at Kyok-Tash Cave”). K4  $\delta^{13}\text{C}$  is interpreted specifically to signify warm growing-season climate with stable precipitation during the earliest Holocene, which coincides with peak June insolation (Fig. 4). Higher NHI is conducive to convective precipitation inland, but the weakened insolation gradient may also have tilted the north-shifted summer westerly jet, favoring positive rainfall anomalies specifically over northwestern Altai and southern Siberia<sup>86,87</sup>. Enhanced contributions from  $^{18}\text{O}$ -enriched JJA rainfall from  $\sim 11.4$  to  $10.5$  ka also explain the heightened magnitude of the K4  $\delta^{18}\text{O}$  peak, relative to the KC  $\delta^{18}\text{O}$  minimum (Fig. 3).

If our hypothesis is correct regarding EH air circulation, the anticorrelated interval in KTC/KC (Fig. 3a) should correspond to relatively warm and wet winters throughout southern West Siberia and Altai, which are favorable to permafrost degradation and peatland expansion. Peatlands were notably absent from the LGM landscape of West Siberia but expanded rapidly following the YD termination<sup>44</sup>. Maximum peatland development and riverine DOC delivery from the Siberian Arctic indeed coincides with the positive K4  $\delta^{18}\text{O}$  excursion from 11.4 to 10.5 ka<sup>11,42,43,80</sup>, reflecting two principal mechanisms that are evidenced by our record. First, eastward retreat of Siberian High influence would have favored winter moisture advection from low-latitude, high- $\delta^{18}\text{O}$  sources (e.g., subtropical Atlantic and Mediterranean), resulting in both warmer and wetter winters over much of Siberia<sup>32,88</sup> (Fig. S8c). Because enhanced snow cover amplifies subsurface warming in boreal climates by insulating ground temperatures from cold extremes, West Siberian permafrost was disproportionately susceptible to the winter circulation anomaly. Second, strengthening and displacement of the summertime westerly jet across southwestern Siberia<sup>86</sup> should simultaneously provoke northerly advection from the Arctic into West Siberia, resulting in cool but humid summer climate. The EH combination of summer sea-ice retreat and global sea-level rise rapidly increased moisture availability from the Arctic, which is a key source region in the modern climatology<sup>23,69,72</sup> (Fig. S10h, i). The confluence of these mechanisms was a relatively stronger increase in mean annual ground temperature and summer moisture balance over the West Siberia and Altai regions, which may explain documented patterns of Siberian permafrost retreat and peatland expansion<sup>34,44</sup>.

In terms of carbon cycling, the metastable permafrost regions near our study site and throughout West Siberia are highly

susceptible to abrupt warming<sup>89,90</sup>, because even small changes in MAAT ( $<1^\circ\text{C}$ ) can melt discontinuous permafrost zones<sup>45</sup> and shift them from a carbon sink to a major carbon source<sup>5,14,44</sup>, which is forecasted to occur under a range of 21st-century scenarios<sup>1,10,12,91</sup>. On the basis of ice-core  $\delta^{13}\text{C}_{\text{CO}_2}$  and geographic surveys, early research hypothesized that thermokarst lakes and peatland methanogenesis accounted for a considerable fraction of the EH peak in  $\text{CH}_4$ <sup>11,40</sup>, emitting up to  $84\text{ Tg CH}_4\text{ yr}^{-1}$  from West Siberian peatlands alone<sup>42</sup>. More recent estimates, however, have disputed the contribution of stored carbon from permafrost landscapes to the EH methane budget ( $<53\text{ Tg CH}_4\text{ yr}^{-1}$ ), based on high-resolution  $\Delta^{14}\text{CH}_4$  data<sup>92,93</sup>. Rather than conclude that permafrost carbon storage may therefore play a minor role in  $\text{CH}_4$  emissions under future anthropogenic warming, we emphasize the contrast of model forecast scenarios with EH climate dynamics. Although summer SAT in Northern Eurasia may have been comparable to recent decades, favoring permafrost degradation and peatland development, predominant circulation regimes and potential influence of the SIS kept summers mild with a relatively high moisture balance. In addition, our data support the contention that winter warming and westerly air circulation likely drove the annual climate signal and spatial heterogeneities across the continental interior, in response to feedbacks in the ocean–cryosphere system<sup>31,32</sup>. Modern anthropogenic warming, however, is driven by an unprecedented rise in GHG concentrations, resulting in a mean annual radiative forcing that will increase both summer and winter SAT well beyond the range of Holocene variability<sup>1–3</sup>. Loss of near-surface permafrost extent (upper 3.5 m) in the northern hemisphere may exceed 37% within a century<sup>1</sup>—a rate not observed during the EH—thereby accelerating DOC loss through soil leaching and destabilization<sup>10</sup>, as well as carbon turnover in permafrost environments<sup>89</sup>. More importantly, abrupt increases in summer SAT will reduce the warm-season moisture balance unless there is a proportional hydrological response, which would strongly alter peatland ecology, water-table depth, and associated carbon fluxes<sup>44</sup>. Finally, we reiterate that the KTC–KC  $\delta^{18}\text{O}$  relationship fundamentally changed between 11.5–10.4 and 9.9–8.9 ka, and only the latter interval is analogous to modern climatologies and recent trends. Based on a comparison of the KTC record with regional paleoclimate data, the EH is not an appropriate analogy for 21st-century projections, without accounting thoroughly for these dynamics.

## Methods

**$^{230}\text{Th}$  dating and age model.** Twelve subsamples of stalagmite K4, each comprised of  $\sim 50\text{ }\mu\text{g}$  of calcite powder, were drilled parallel to growth laminae (Fig. S2a) and  $^{230}\text{Th}$ -dated for construction of an age-depth model. A 1 mm carbide dental drill bit was used to sample each powder. Procedures for chemical separation and purification of U and Th are described in Shen et al.<sup>94</sup>. Dating was performed at the High-Precision Mass Spectrometry and Environment Change Laboratory, Department of Geosciences, National Taiwan University. A Thermo-Fisher Neptune multi-collector inductively coupled plasma mass spectrometer (MC-ICP-MS) with a secondary electron multiplier was used for the determination of the U–Th isotopic contents and compositions<sup>94,95</sup>. The decay constants of  $^{230}\text{Th}$ ,  $^{234}\text{U}$ , and  $^{238}\text{U}$  are  $9.1705 \times 10^{-6}\text{ yr}^{-1}$ ,  $2.82206 \times 10^{-6}\text{ yr}^{-1}$ , and  $1.55125 \times 10^{-10}\text{ yr}^{-1}$ , respectively<sup>95,96</sup>. The age correction for the initial  $^{230}\text{Th}$  was performed using the average crustal  $^{230}\text{Th}/^{232}\text{Th}$  ratio of  $4.4 \pm 2.2 \times 10^{-6}$  from Taylor and McLennan<sup>97</sup>. All ages are reported as “ka b2k” (kiloannum before 2000 C.E.). Error bars for  $^{230}\text{Th}$  dates signify  $2\sigma$  analytical uncertainties (Table S1).

We constructed the age-depth chronology of K4 by two models: linear interpolation and a Monte Carlo approach using MOD-AGE<sup>52</sup>. Because of the high precision and sufficient dating coverage in this time window, the difference of modeled ages between these two approaches is negligible (0–14.5 years) (Fig. S2b). We used MOD-AGE to build the final chronology for the K4 record.

**Stable-isotope and elemental analysis of stalagmite K4.** Stalagmite K4 was cut along the growth axis and polished before sampling carbonate powders every 0.1 mm using a micro milling device in National Taiwan University.  $\delta^{18}\text{O}$  and  $\delta^{13}\text{C}$  were determined by phosphoric-acid reaction at  $70^\circ\text{C}$  in a Kiel IV automated carbonate preparation device coupled to a Thermo-Fisher MAT253 mass



spectrometer at the Beijing Createch Testing Technology Co., Ltd, China.  $\delta^{18}\text{O}$  and  $\delta^{13}\text{C}$  were corrected with internal and external standards, and precision is better than 0.08‰ and 0.06‰, respectively. Values are reported as per mil (‰) deviations from the V-PDB standard (Supplementary Data 1). The concentrations of elements Mg and Ca were determined by high-performance micro area X-Ray Fluorescence spectrometer (Bruker/M4 Tornado) at a spatial interval of 50  $\mu\text{m}$  in the State Key Laboratory for Mineral Deposits Research, Nanjing University (Supplementary Data 1).

### Data availability

Stable-isotope, trace-element, and U-series data that support the findings of this study have been deposited in the NOAA Paleoclimatology Data online repository at <https://www.ncdc.noaa.gov/paleo/study/33713> and are available within the Supplementary Materials and Supplementary Data 1. Modeled precipitation  $\delta^{18}\text{O}$  data that support the findings of this study are accessible from the IsoGSM2 database: <http://isotope.iis.u-tokyo.ac.jp/~kei/tmp/isogsm2/>.

Received: 16 January 2021; Accepted: 22 July 2021;

Published online: 29 September 2021

### References

- Pachauri, R. K. et al. *Climate Change 2014: Synthesis Report. Contribution of Working Groups I, II and III to the Fifth Assessment Report of the Intergovernmental Panel on Climate Change*. (Ipc, 2014).
- Marcott, S. A., Shakun, J. D., Clark, P. U. & Mix, A. C. A reconstruction of regional and global temperature for the past 11,300 years. *Science* **339**, 1198–1201 (2013).
- Kaufman, D. et al. A global database of Holocene paleotemperature records. *Sci. Data* **7**, <https://doi.org/10.1038/s41597-020-0445-3> (2020).
- Zhang, Y. et al. Projections of glacier change in the Altai Mountains under twenty-first century climate scenarios. *Clim. Dyn.* **47**, 2935–2953 (2016).
- Hugelius, G. et al. Large stocks of peatland carbon and nitrogen are vulnerable to permafrost thaw. *Proc. Natl Acad. Sci.* **117**, 20438–20446 (2020).
- Schuur, E. A. G. et al. Vulnerability of permafrost carbon to climate change: implications for the global carbon cycle. *BioScience* **58**, 701–714 (2008).
- Romanovsky, V. E. et al. Past and recent changes in air and permafrost temperatures in eastern Siberia. *Global Planet. Change* **56**, 339–413 (2007).
- Romanovsky, V. E. et al. Thermal State of Permafrost in Russia. *Permafrost. Periglac. Process.* **21**, 136–155 (2010).
- Karlsson, J. M. et al. Thermokarst lake, hydrological flow and water balance indicators of permafrost change in Western Siberia. *J. Hydrol.* **464**–**465**, 459–466 (2012).
- Frey, K. E. & Smith, L. C. Amplified carbon release from vast West Siberian peatlands by 2100. *Geophys. Res. Lett.* **32**, <https://doi.org/10.1029/2004GL020205> (2005).
- MacDonald, G. M. et al. Rapid early development of circumarctic peatlands and atmospheric  $\text{CH}_4$  and  $\text{CO}_2$  variations. *Science* **314**, 285–288 (2006).
- Grosse, G. et al. Vulnerability and feedbacks of permafrost to climate change. *Eos, Trans. Am. Geophys. Union* **92**, 73–74 (2011).
- Wild, B. et al. Rivers across the Siberian Arctic unearth the patterns of carbon release from thawing permafrost. *Proc. Natl Acad. Sci.* **116**, 10280–10285 (2019).
- Turetsky, M. R. et al. Carbon release through abrupt permafrost thaw. *Nat. Geosci.* **13**, 138–143 (2020).
- Aizen, E. M. et al. Abrupt and moderate climate changes in the mid-latitudes of Asia during the Holocene. *J. Glaciol.* **62**, 411–439 (2016).
- Cheng, H. et al. Climate variations of Central Asia on orbital to millennial timescales. *Sci. Rep.* **6**, 36975 (2016).
- Rao, Z. et al. Long-term summer warming trend during the Holocene in central Asia indicated by alpine peat  $\alpha$ -cellulose  $\delta^{13}\text{C}$  record. *Quat. Sci. Rev.* **203**, 56–67 (2019).
- Cheung, H. N. et al. Observational climatology and characteristics of wintertime atmospheric blocking over Ural–Siberia. *Clim. Dyn.* **41**, 63–79 (2013).
- Li, Y. & Morrill, C. A Holocene East Asian winter monsoon record at the southern edge of the Gobi Desert and its comparison with a transient simulation. *Clim. Dyn.* **45**, 1219–1234 (2015).
- Cohen, J. et al. Recent Arctic amplification and extreme mid-latitude weather. *Nat. Geosci.* **7**, 627–637 (2014).
- Stieglitz, M., Déry, S., Romanovsky, V. E. & Osterkamp, T. The role of snow cover in the warming of Arctic permafrost. *Geophys. Res. Lett.* **30**, 54–1 (2003).
- Kitover, D. C., Renssen, H., van Balen, R., Vandenbergh, J. & Roche, D. M. Coupling of VAMPERS within iLOVECLIM: experiments during the LGM and last deglaciation. *J. Quat. Sci.* **34**, 215–227 (2019).
- Malygina, N., Papina, T., Kononova, N. & Barlyaeva, T. Influence of atmospheric circulation on precipitation in Altai Mountains. *J. Mountain Sci.* **14**, 46–59 (2017).
- Marshall, G. J. Decadal variability in the impact of atmospheric circulation patterns on the winter climate of northern Russia. *J. Clim.* **34**, 1005–1021 (2021).
- Frey, K. E. & Smith, L. C. Recent temperature and precipitation increases in West Siberia and their association with the Arctic Oscillation. *Polar Res.* **22**, 287–300 (2003).
- Cohen, J. et al. Divergent consensus on Arctic amplification influence on midlatitude severe winter weather. *Nat. Clim. Change* **10**, 20–29 (2019).
- Mori, M. et al. A reconciled estimate of the influence of Arctic sea-ice loss on recent Eurasian cooling. *Nat. Clim. Change* **9**, 123–129 (2019).
- Screen, J. A., Simmonds, I., Deser, C. & Tomas, R. The atmospheric response to three decades of observed Arctic Sea ice loss. *J. Clim.* **26**, 1230–1248 (2013).
- Woollings, T., Harvey, B. & Masato, G. Arctic warming, atmospheric blocking and cold European winters in CMIP5 models. *Environ. Res. Lett.* **9**, 014002 (2014).
- Park, H.-S. et al. The impact of Arctic sea ice loss on mid-Holocene climate. *Nat. Commun.* **9**, <https://doi.org/10.1038/s41467-018-07068-2> (2018).
- Meyer, H. et al. Long-term winter warming trend in the Siberian Arctic during the mid- to late Holocene. *Nat. Geosci.* **8**, 122–125 (2015).
- Baker, J. L., Lachniet, M. S., Chervyatsova, O., Asmerom, Y. & Polyak, V. J. Holocene warming in western continental Eurasia driven by glacial retreat and greenhouse forcing. *Nat. Geosci.* **10**, 430–435 (2017).
- Rao, Z. et al. Long-term winter/summer warming trends during the Holocene revealed by  $\alpha$ -cellulose  $\delta^{18}\text{O}/\delta^{13}\text{C}$  records from an alpine peat core from central Asia. *Quat. Sci. Rev.* **232**, 106217 (2020).
- Vaks, A. et al. Palaeoclimate evidence of vulnerable permafrost during times of low sea ice. *Nature* **577**, 221–225 (2020).
- Shakun, J. D. et al. Global warming preceded by increasing carbon dioxide concentrations during the last deglaciation. *Nature* **484**, 49–54 (2012).
- Berben, S. M. P., Husum, K., Navarro-Rodriguez, A., Belt, S. T. & Aagaard-Sørensen, S. Semi-quantitative reconstruction of early to late Holocene spring and summer sea ice conditions in the northern Barents Sea. *J. Quat. Sci.* **32**, 587–603 (2017).
- Xiao, X. et al. Deglacial and Holocene sea-ice variability north of Iceland and response to ocean circulation changes. *Earth Planet. Sci. Lett.* **472**, 14–24 (2017).
- Monnin, E. et al. Evidence for substantial accumulation rate variability in Antarctica during the Holocene, through synchronization of  $\text{CO}_2$  in the Taylor Dome, Dome C and DML ice cores. *Earth Planet. Sci. Lett.* **224**, 45–54 (2004).
- Beck, J. et al. Bipolar carbon and hydrogen isotope constraints on the Holocene methane budget. *Biogeosciences* **15**, 7155–7175 (2018).
- Walter, K. M., Edwards, M. E., Grosse, G., Zimov, S. A. & Chapin, F. S. Thermokarst lakes as a source of atmospheric  $\text{CH}_4$  during the last deglaciation. *Science* **318**, 633–636 (2007).
- Katsuta, N. et al. Siberian Permafrost thawing accelerated at the Bølling/Allerød and preboreal warm periods during the last deglaciation. *Geophys. Res. Lett.* **46**, 13961–13971 (2019).
- Smith, L. C. et al. Siberian peatlands a net carbon sink and global methane source since the early holocene. *Science* **303**, 353–356 (2004).
- Tesi, T. et al. Massive remobilization of permafrost carbon during post-glacial warming. *Nat. Commun.* **7**, <https://doi.org/10.1038/ncomms13653> (2016).
- Alexandrov, G. A., Brovkin, V. A. & Kleinen, T. The influence of climate on peatland extent in Western Siberia since the Last Glacial Maximum. *Sci. Rep.* **6**, <https://doi.org/10.1038/srep24784> (2016).
- Vaks, A. et al. Speleothems reveal 500,000-year history of Siberian permafrost. *Science* **340**, 183–186 (2013).
- Lechleitner, F. A. et al. Permafrost-related hiatuses in stalagmites: evaluating the potential for reconstruction of carbon cycle dynamics. *Quat. Geochronol.* **56**, 101037 (2020).
- Davis, B. A. S. & Brewer, S. Orbital forcing and role of the latitudinal insolation/temperature gradient. *Clim. Dyn.* **32**, 143–165 (2009).
- Dyke, A. S. An outline of North American deglaciation with emphasis on central and northern Canada. *Developments in Quaternary Science*, **2**, 373–424 (2004).
- Stroeven, A. P. et al. Deglaciation of Fennoscandia. *Quat. Sci. Rev.* **147**, 91–121 (2016).
- Zhang, Y. et al. Glacier mass balance and its potential impacts in the Altai Mountains over the period 1990–2011. *J. Hydrol.* **553**, 662–677 (2017).
- Li, Y. et al. Temporal-spatial variability of modern climate in the Altai Mountains during 1970–2015. *PLoS ONE* **15**, e0230196 (2020).
- Hercman, H. & Pawlak, J. MOD-AGE: an age-depth model construction algorithm. *Quat. Geochronol.* **12**, 1–10 (2012).
- Fohlmeister, J. et al. Main controls on the stable carbon isotope composition of speleothems. *Geochimica et Cosmochimica Acta* **279**, 67–87 (2020).

54. Tremaine, D. M., Froelich, P. N. & Wang, Y. Speleothem calcite formed in situ: Modern calibration of  $\delta^{18}\text{O}$  and  $\delta^{13}\text{C}$  paleoclimate proxies in a continuously-monitored natural cave system. *Geochimica et Cosmochimica Acta* **75**, 4929–4950 (2011).
55. Thornthwaite, C. W. An approach toward a rational classification of climate. *Geogr. Rev.* **38**, 55–94 (1948).
56. Kalnay, E. et al. The NCEP/NCAR 40-year reanalysis project. *Bull. Am. Meteorol. Soc.* **77**, 437–472 (1996).
57. Bueh, C. & Nakamura, H. Scandinavian pattern and its climatic impact. *Q. J. R. Meteorol. Soc.* **133**, 2117–2131 (2007).
58. Wang, T. et al. A climatological interpretation of precipitation  $\delta^{18}\text{O}$  across Siberia and Central Asia. *Water* **12**, <https://doi.org/10.3390/w12082132> (2020).
59. Bothe, O., Fraedrich, K. & Zhu, X. Precipitation climate of Central Asia and the large-scale atmospheric circulation. *Theor. Appl. Climatol.* **108**, 345–354 (2012).
60. Breitenbach, S. et al. Holocene interaction of maritime and continental climate in Central Europe: new speleothem evidence from Central Germany. *Global Planet. Change* **176**, 144–161 (2019).
61. Yoshimura, K., Kanamitsu, M., Noone, D. & Oki, T. Historical isotope simulation using Reanalysis atmospheric data. *J. Geophys. Res.: Atmospheres* **113**, <https://doi.org/10.1029/2008JD010074> (2008).
62. Lachniet, M. S. Climatic and environmental controls on speleothem oxygen-isotope values. *Quat. Sci. Rev.* **28**, 412–432 (2009).
63. Baker, A. et al. Global analysis reveals climatic controls on the oxygen isotope composition of cave drip water. *Nat. Commun.* **10**, 2984 (2019).
64. Domínguez-Villar, D., Lojen, S., Krklec, K., Baker, A. & Fairchild, I. J. Is global warming affecting cave temperatures? Experimental and model data from a paradigmatic case study. *Clim. Dyn.* **45**, 569–581 (2014).
65. Rau, G. et al. Controls on cave drip water temperature and implications for speleothem-based paleoclimate reconstructions. *Quat. Sci. Rev.* **127**, 19–36 (2015).
66. Domínguez-Villar, D., Krklec, K., López-Sáez, J., & Sierro, F. Thermal impact of Heinrich stadials in cave temperature and speleothem oxygen isotope records. *Quat. Res.* 1–14, <https://doi.org/10.1017/qua.2020.99> (2020).
67. Guo, X. et al. Response of drip water temperature to climate variability: a case study in Xiaoyan Cave, southwest China. *Hydrol. Sci. J.* **64**, 873–884 (2019).
68. Dansgaard, W. Stable isotopes in precipitation. *Tellus* **16**, 436–468 (1964).
69. Kostrova, S. S., Meyer, H., Fernandoy, F., Werner, M. & Tarasov, P. E. Moisture origin and stable isotope characteristics of precipitation in southeast Siberia. *Hydrol. Process.* **34**, 51–67 (2020).
70. Butzin, M. et al. Variations of oxygen-18 in West Siberian precipitation during the last 50 years. *Atmos. Chem. Phys.* **14**, 5853–5869 (2014).
71. Bühler, J. C. et al. Comparison of the oxygen isotope signatures in speleothem records and iHadCM3 model simulations for the last millennium. *Clim. Past Discuss.* **2020**, 1–30 (2020).
72. Kurita, N. Modern isotope climatology of Russia: a first assessment. *J. Geophys. Res.* **109**, <https://doi.org/10.1029/2003jd003404> (2004).
73. Rozanski, K., Araguás-Araguás, L. & Gonfiantini, R. Relation between long-term trends of oxygen-18 isotope composition of precipitation and climate. *Science* **258**, 981–985 (1992).
74. Wu, D. et al. Peat brGDGTs-based Holocene temperature history of the Altai Mountains in arid Central Asia. *Palaeogeogr., Palaeoclim., Palaeoecol.* **538**, 109464 (2020).
75. Wang, W. & Zhang, D. Holocene vegetation evolution and climatic dynamics inferred from an ombrotrophic peat sequence in the southern Altai Mountains within China. *Global Planet. Change* **179**, 10–22 (2019).
76. Liu, X. et al. Variations in the oxygen isotopic composition of precipitation in the Tianshan Mountains region and their significance for the Westerly circulation. *J. Geogr. Sci.* **25**, 801–816 (2015).
77. Wang, L. et al. Effect of the climate shift around mid 1970s on the relationship between wintertime Ural blocking circulation and East Asian climate. *Int. J. Climatol.* **30**, 153–158 (2010).
78. Nesje, A., Dahl, S. O. & Bakke, J. Were abrupt Lateglacial and early-Holocene climatic changes in northwest Europe linked to freshwater outbursts to the North Atlantic and Arctic Oceans? *Holocene* **14**, 299–310 (2004).
79. Winterfeld, M. et al. Deglacial mobilization of pre-aged terrestrial carbon from degrading permafrost. *Nat. Commun.* **9**, <https://doi.org/10.1038/s41467-018-06080-w> (2018).
80. Martens, J. et al. Remobilization of dormant carbon from Siberian-Arctic permafrost during three past warming events. *Sci. Adv.* **6**, eabb6546 (2020).
81. Mayewski, P. A. et al. Holocene climate variability. *Quat. Res.* **62**, 243–255 (2004).
82. Tarasov, P. et al. Vegetation and climate dynamics during the Holocene and Eemian interglacials derived from Lake Baikal pollen records. *Palaeogeogr., Palaeoclim., Palaeoecol.* **252**, 440–457 (2007).
83. Rudaya, N. et al. Holocene environments and climate in the Mongolian Altai reconstructed from the Hoto-Nur pollen and diatom records: a step towards better understanding climate dynamics in Central Asia. *Quat. Sci. Rev.* **28**, 540–554 (2009).
84. Blyakharchuk, T. A., Wright, H. E., Borodavko, P. S., van der Knaap, W. O. & Ammann, B. Late Glacial and Holocene vegetational changes on the Ulagan high-mountain plateau, Altai Mountains, southern Siberia. *Palaeogeogr., Palaeoclim., Palaeoecol.* **209**, 259–279 (2004).
85. Zhang, D. & Feng, Z. Holocene climate variations in the Altai Mountains and the surrounding areas: a synthesis of pollen records. *Earth-Sci. Rev.* **185**, 847–869 (2018).
86. Herzschuh, U. et al. Position and orientation of the westerly jet determined Holocene rainfall patterns in China. *Nat. Commun.* **10**, 2376 (2019).
87. Huang, C. et al. Holocene summer temperature in arid central Asia linked to millennial-scale North Atlantic climate events and driven by centennial-scale solar activity. *Palaeogeogr., Palaeoclim., Palaeoecol.* **556**, 109880 (2020).
88. Persoiu, A., Ionita, M. & Weiss, H. Atmospheric blocking induced by the strengthened Siberian High led to drying in west Asia during the 4.2 ka BP event—a hypothesis. *Clim. Past* **15**, 781–793 (2019).
89. Dean, J. F. et al. East Siberian Arctic inland waters emit mostly contemporary carbon. *Nat. Commun.* **11**, <https://doi.org/10.1038/s41467-020-15511-6> (2020).
90. Lawrence, D. M. & Slater, A. G. A projection of severe near-surface permafrost degradation during the 21st century. *Geophys. Res. Lett.* **32**, L2440 (2005).
91. Vendenbergh, J. et al. Eurasian permafrost instability constrained by reduced sea-ice cover. *Quat. Sci. Rev.* **34**, 16–23 (2012).
92. Dyonisius, M. N. et al. Old carbon reservoirs were not important in the deglacial methane budget. *Science* **367**, 907–910 (2020).
93. Petrenko, V. V. et al. Minimal geological methane emissions during the Younger Dryas–Preboreal abrupt warming event. *Nature* **548**, 443–446 (2017).
94. Shen, C.-C. et al. High-precision and high-resolution carbonate  $^{230}\text{Th}$  dating by MC-ICP-MS with SEM protocols. *Geochimica et Cosmochimica Acta* **99**, 71–86 (2012).
95. Cheng, H. et al. Improvements in  $^{230}\text{Th}$  dating,  $^{230}\text{Th}$  and  $^{234}\text{U}$  half-life values, and U–Th isotopic measurements by multi-collector inductively coupled plasma mass spectrometry. *Earth Planet. Sci. Lett.* **371**–372, 82–91 (2013).
96. Jaffey, A. H., Flynn, K. F., Glendenin, L. E., Bentley, W. C. & Essling, A. M. Precision measurement of half-lives and specific activities of  $\delta^{235}\text{U}$  and  $\delta^{238}\text{U}$ . *Phys. Rev. C* **4**, 1889–1906 (1971).
97. Taylor, S. R. & McLennan, S. M. The geochemical evolution of the continental crust. *Rev. Geophys.* **33**, 241–265 (1995).

## Acknowledgements

This research was supported by the National Natural Science Foundation of China (NSFC, No. 41772170; 42011530078; 42172204), and the Fundamental Research Funds for the Central Universities, China (No. XDJK2017A010 and No. XDJK2020D005) to T.-Y.L., as well as grant NSFC 41888101 to J.L.B. and H.C. Grant MOST 106-2923-M-002-002-MY3 from Taiwan to H.-C.L. supported the fieldwork. Fieldwork was further supported by Russian Foundation of Basic Research Grant No. 20-55-53015/20 and budget theme INCES SB RAS No AAAAAA-A16-116041356666-6 to T.B. U-Th dating at the High-Precision Mass Spectrometry and Environment Change Laboratory (HISPEC), Department of Geosciences was supported by grants from the Science Vanguard Research Program of the Ministry of Science and Technology (MOST), Taiwan, ROC (108-2119-M-002-012), the Higher Education Sprout Project of the Ministry of Education, Taiwan, ROC (108L901001), and the National Taiwan University (109L8926) to C.-C.S. This work was partially supported by U.S. NSF Grant 1702816 to R.L.E. We are grateful to Kei Yoshimura for allowing and reviewing our use of the IsoGSM2 database in the modern climate analyses. NCEP Reanalysis data provided by the NOAA/OAR/ESRL PSL, Boulder, Colorado, USA, from <https://psl.noaa.gov>. Global Network of Isotopes in Precipitation (GNIP) data referenced herein were accessed from the IAEA/WMO (2020) database at <https://www.iaea.org/services/networks/gnip>. Russian meteorological data were accessed from <http://meteo.ru/data> (2020).

## Author contributions

T.-Y.L., H.-C.L. and T.B. designed the research. T.-Y.L. and J.L.B. wrote the manuscript. T.W., Y.W. J.Z., X.-G.K., and W.-L.X. contributed to instrumental measurements and the  $^{230}\text{Th}$  dating work. T.-L.Y., C.-C.S., H.C. and R.L.E. provided technical support in  $^{230}\text{Th}$  dating work. All authors discussed the results and contributed to the final manuscript and figures.

## Competing interests

The authors declare no competing interests.

## Additional information

**Supplementary information** The online version contains supplementary material available at <https://doi.org/10.1038/s43247-021-00238-z>.

**Correspondence** and requests for materials should be addressed to Ting-Yong Li, Hong-Chun Li or Tatiana Blyakharchuk.

**Peer review information** *Communications Earth & Environment* thanks Aurel Perşoiu, Jef Vandenberghe, and the other, anonymous, reviewer(s) for their contribution to the peer review of this work. Primary Handling Editors: Joe Aslin, Clare Davis.

**Reprints and permission information** is available at <http://www.nature.com/reprints>

**Publisher's note** Springer Nature remains neutral with regard to jurisdictional claims in published maps and institutional affiliations.



**Open Access** This article is licensed under a Creative Commons Attribution 4.0 International License, which permits use, sharing, adaptation, distribution and reproduction in any medium or format, as long as you give appropriate credit to the original author(s) and the source, provide a link to the Creative Commons license, and indicate if changes were made. The images or other third party material in this article are included in the article's Creative Commons license, unless indicated otherwise in a credit line to the material. If material is not included in the article's Creative Commons license and your intended use is not permitted by statutory regulation or exceeds the permitted use, you will need to obtain permission directly from the copyright holder. To view a copy of this license, visit <http://creativecommons.org/licenses/by/4.0/>.

© The Author(s) 2021